Biosensors and Bioelectronics 164 (2020) 112320

Contents lists available at ScienceDirect

Biosensors and Bioelectronics

journal homepage: http://www.elsevier.com/locate/bios

A chemiresistive biosensor based on a layered graphene oxide/graphene composite for the sensitive and selective detection of circulating miRNA-21

Chi-Hsien Huang *, Tzu-Ting Huang, Chia-Heng Chiang, Wei-Ting Huang, Yi-Ting Lin

Department of Materials Engineering, Ming Chi University of Technology, New Taipei City, 24301, Taiwan, ROC

ARTICLE INFO

Keywords:
Graphene
miRNA
Chemiresistive biosensor
π–π interaction
Cancer
Atomic layer oxidation

ABSTRACT

In this study we developed a uniform, large-area, layered graphene composite of graphene oxide/graphene (GO/G) for the detection of circulating miRNA-21, a reliable biomarker for early cancer diagnosis. We prepared this layered composite of GO/G through low-damage plasma treatment of bilayer G. The top layer of G was oxidized (i.e., atomic layer oxidation) to form a GO layer, which acted as the bio-receptor, while retaining the properties of the bottom layer of G, which acted as an electrical response medium. With this structure, we fabricated a simple chemiresistive biosensor that could detect miRNA-21. The electrical resistance of the sensor varied linearly ($R^2 = 0.986$) with respect to concentrations of the target miRNA-21 in the range from 10 pM to 100 nM in phosphate-buffered saline (PBS); the limit of detection was 14.6 pM. Hall measurements revealed that the mobility and concentration of the hole carriers both decreased upon increasing the target concentration, leading to the measured increase in resistivity of our chemiresistive biosensor. Furthermore, the sensor could discriminate the complementary target miRNA-21 from its single- and four-base-mismatched counterparts and another non-complementary miRNA. The ability to detect miRNA-21 in human serum albumin and bovine serum albumin was almost identical to that in PBS.

1. Introduction

Because cancer is one of the leading causes of human death worldwide, the quest remains to develop reliable and sensitive methods for its early detection and diagnosis. MicroRNAs (miRNAs), small non-coding molecules of RNA comprising approximately 22 nucleotides, are highly correlated to cancer initiation, oncogenesis, and tumor responses to treatment (Xia et al., 2015; Jansson et al., 2012). Among the many reported sequences of miRNAs, miRNA-21 has been identified as the only miRNA overexpressed in 11 types of solid tumors, making it a good candidate as a biomarker for clinical diagnosis (Hong et al., 2013). At present, miRNA-21 can be detected using several techniques based on, for example, Northern blotting, in situ hybridization, the real-time polymerase chain reaction (RT-PCR), sequencing, and microarrays (Kim et al., 2010; Ouyang et al., 2019). Among them, Northern blotting and in situ hybridization are used most widely as standard methods, but they have several drawbacks, including low sensitivity, tedious protocols, and time-consumption. Although RT-PCR can be a simple and practical method, it can be expensive and inconvenient when applied to point-of-care testing. Sequencing is employed widely for the classification and analysis of many miRNAs, providing substantial genetic information with high accuracy, but it is not suitable for large-scale use in early diagnosis because it is a slow and expensive process. Although microarray technologies enable rapid analyses and diagnoses, they come with low sensitivity and selectivity. To improve the sensitivity, selectivity, and limit of detection (LOD), DNA hybridization detection—using, for example, electrical, optical, and electrochemical biosensors—has been developed for use in point-of-care platforms for miRNA detection (Dong et al., 2010; Wang et al., 2019a; Salahandish et al., 2018). In addition, chemiresistive biosensors have been developed displaying performance similar to that of systems based on DNA hybridization. Because of their simplicity, ease of read-out, and low cost, such biosensors have great potential in the development of portable devices for point-of-care testing and advancing human healthcare. The materials that function as transducers in biosensors operate as physically or covalently immobilized recognition elements. Upon biorecognition of, for example, DNA, antibodies, enzymes, aptamers, or ligands, the transducer translates the physical or chemical change to a signal output (Qian et al., 2019). Since its discovery by Geim and Novoselov (Novoselov et al., 2004), graphene (G) has been employed widely in various

* Corresponding author.
E-mail address: chhuang@mail.mcut.edu.tw (C.-H. Huang).

https://doi.org/10.1016/j.bios.2020.112320
Received 16 February 2020; Received in revised form 14 May 2020; Accepted 20 May 2020
Available online 27 May 2020
0956-5663/© 2020 Elsevier B.V. All rights reserved.

types of biosensors, which take advantage of its excellent conductivity, good biocompatibility, high mechanical strength, and high surface area (Zhang et al., 2019; Wang et al., 2019b; Huang et al., 2011). As an atomic-layer-thick two-dimensional (2D) material, G is very promising for use as a transducer in biosensors because of its high sensitivity toward the attachment or bonding of foreign atoms or molecules. In practice, however, the inertness of G has meant that graphene oxide (GO)—an oxidized derivative—is more suitable for use as a transducer for conjugation with various biorecognition elements. GO possesses oxygen atoms—primarily in the forms of OH, CO_2H, and epoxide groups—that enhance its chemical reactivity. Among these functional groups, CO_2H groups can react with the amino groups of the aforementioned recognition elements to form stable covalent amide bonds (Cheng et al., 2017; Justino et al., 2017; Liang et al., 2013). Nevertheless, GO is commonly prepared through Hummer's method, which produces nonuniform GO sheets in which the number of layers of GO is not easy to control. In addition, the presence of covalently bonded oxygen atoms can destroy the lattice structure, thereby potentially losing some of the attractive properties of G. Although functionalization of G with various materials can be achieved noncovalently (through π–π interactions and van der Waals forces) without disrupting its physical properties, such physical adsorption processes are nonspecific and often lead to noisy signals (Park et al., 2016).

In this study, we prepared a simple chemiresitive biosensor based on a layered composite of GO/G as a transducer; it combined the high chemical reactivity of the top layer of GO with the high conductivity of the bottom layer of G. We prepared this GO/G structure through an atomic oxidation process: low-damage plasma treatment (LDPT) on bilayer graphene (BiG). Only the top layer of BiG was oxidized through LDPT, leaving the bottom layers unchanged. The top layer of GO provided the active sites for forming covalent bonds with the recognition element—in this case, target miRNA; furthermore, the conductivity of the bottom layer of G was altered upon attachment (through π–π interactions) of the target miRNA. The detection of miRNA-21 was characterized by an increase in the resistance of the GO/G-based chemiresistive biosensor. The resistance of the biosensor increased linearly upon increasing the concentration of miRNA-21 in phosphate-buffered saline (PBS). We performed Hall measurements to identify the origin of this phenomenon. We demonstrated the importance of the π–π interactions between the GO and G layers through measurements using stacked double layers of G, instead of the BiG, oxidized through LDPT. We evaluated the selectivity of the biosensor against single- and four-base mismatches of miRNA-21 and another non-complementary miRNA. In addition, we could also detect miRNA-21 diluted in human serum albumin (HSA) and bovine serum albumin (BSA), thereby mimicking real sample testing.

2. Experimental

2.1. Materials and instrumentation

The high-performance liquid chromatography (HPLC)–purified DNA probes and target RNAs used in this study were purchased from Geomics Company (New Taipei City, Taiwan); their sequences are presented in Table S1. The DNA probes and RNAs contained 22 base pairs (bp); they were dissolved and diluted in 1x PBS buffer (pH 7.4). HSA and BSA were purchased from Sigma–Aldrich and Gibco Life Technologies, respectively. All other solvents and reagents were of analytical grade and used as received.

The chemical compositions of BiG and GO/G were examined using X-ray photoelectron spectroscopy (XPS; VG ESCA Scientific Theta Probe) and a monochromated Al Kα source. Raman spectra were collected using a Horiba iHR-550 Raman system. The Si peak at 520 cm^{-1} was used as the reference for wavenumber calibration prior to each measurement. The hydrophilicities of the samples were investigated in terms of contact angles (CAs) of droplets of deionized water, measured using a PSC-100B instrument (Pentad Scientific). Five or more samples were subjected to measurement; average CAs with errors of one standard deviation are reported herein. The electrical properties of the GO/G samples were recorded using a Hall effect measurement system (AHM-800B, Agilent, USA).

2.2. BiG and GO/G

Single layer graphene (SLG) was grown on copper foil through chemical vapor deposition (CVD) in a 3-inch-diameter tubular quartz furnace. The copper foil was placed at the center of the quartz tube and then the furnace temperature was ramped up to 1040 °C under a constant flow of H_2 at 1 torr for 50 min. The copper foil was annealed at 1040 °C for 30 min to eliminate any organic matter and native oxide from its surface. A gas mixture of CH_4 (60 sccm) and H_2 (15 sccm) was introduced into the system at 1040 °C; the pressure was maintained at 1 torr for 20 min for growth of the SLG. The furnace was then rapidly cooled to room temperature. The as-grown G was transferred from the copper foil to a thermally grown 300-nm silicon dioxide–atop–silicon substrate (SiO_2/Si), using the poly(methyl methacrylate) (PMMA) method, to obtain a sample of SLG on SiO_2/Si (SLG/SiO_2/Si). Details of G-transfer method are available elsewhere (Huang et al., 2018). The SLG/SiO_2/Si samples were annealed under vacuum at 300 °C for 30 min to remove any organic residues remaining after the transfer process. The G was also transferred from copper foil onto the above-mentioned SLG/SiO_2/Si by repeating the transfer method to obtain stacked double layer graphene (DLG). Finally, the stacked DLG samples were annealed again to obtain BiG on SiO_2/Si.

After the preparation of BiG on SiO_2/Si, the samples were subjected to LDPT with a mixture of O_2 and H_2 gases to obtain a high density of CO_2H groups on the G surface (Cheng et al., 2016). An inductively coupled plasma (ICP) source was used to generate the high-density plasma. A complementary filter was inserted between the plasma source and the samples, as displayed schematically in Fig. S1. With this filter, plasma damage resulting from UV irradiation and ion bombardment was efficiently minimized to realize the LDPT process. In effect, only the top layer of the BiG was oxidized, thereby retaining the physical and chemical properties of the bottom layer, and forming GO/G layered composites (Huang et al., 2014). The following processing conditions were used: radio frequency, 13.56 MHz; power, 200 W; process pressure, 0.2 torr; substrate temperature, 25 °C; treatment time, 25 min.

2.3. Sensor fabrication and miRNA-21 detection protocol

An interdigitated Cr (5 nm)/Au (50 nm) electrode was deposited using a thermal evaporator onto the SiO_2/Si substrate through a shadow mask. Fig. S2(a) provides schematic representations of the geometries of the interdigitated electrode and the device. Next, the BiG was transferred onto the Cr/Au-deposited SiO_2/Si substrate by repeating the transfer process described in Section 2.1. The sensing area of the sensor was defined to be a square of 1 cm^2 by using an epoxy resin–type adhesive dispensed by an automatic *x*–*y* stage packager. The samples of BiG on the interdigitated electrode were treated through LDPT to form GO/G layered composites. Immediately after performing LDPT to complete the sensor fabrication process, the DNA probes were immobilized on the GO/G sample through carbodiimide-mediated reactions (amide bond formation) between the amino groups of DNA and the CO_2H groups of GO. A drop of 100 nM DNA was placed on the sensing region encapsulated by epoxy and left at room temperature for 16 h; this sample served as the probe for target RNA detection. The excess non-bonded DNA was washed away with 1x PBS buffer. Fig. S2(b) displays the device scheme and a real device ready for targeting miRNA-21. Solutions of target miRNAs of various concentrations in PBS were dispensed onto the sensing region to hybridize with the DNA probes at room temperature for 6 h. The samples were then rinsed with PBS to remove the excess of the target RNAs. The selectivity of the sensors was

evaluated using single- and four-base-mismatched samples and non-complementary miRNAs, using the same sensor fabrication and detection protocols. miRNA-21 solutions were also prepared in the presence of HSA and BSA to evaluate the practical applicability of the detection platform to calculate the electrical resistances of the sensors in the presence of various concentrations of the target RNAs, current–voltage (*I–V*) curves were measured under ambient conditions using an Agilent B1500 system. The sensor response was defined as the variation in resistance

$$\frac{(R - R_0)}{R_0} \times 100\% \quad (1)$$

where R_0 and R represent the electrical resistances of the sensor before and after hybridization, respectively. The performance of at least five sensors was measured; average data and standard deviations are reported herein.

3. Results and discussion

3.1. Characterization of GO/G

Raman spectroscopy is a powerful, rapid, and non-destructive technique for characterizing G sheets (Ni et al., 2008; Casiraghi et al., 2007). Fig. 1(a) displays the Raman spectra of the SLG; the G-band (ca. 1585 cm^{-1}) and a 2D-band (ca. 2680 cm^{-1}) represent the sp^2-hybridized C–C bonds, while the D-band (ca. 1345 cm^{-1}) represents non-sp^2-hybridized C atoms arising from atomic-scale defects. The intensity ratio (I_{2D}/I_G) of the 2D- and G-bands was approximately 2.2; the D-band was almost invisible. Fig. 1(b) presents the transmittance spectrum of the SLG. The transmittance of the SLG at 550 nm was 97.6%, very close to that reported in the literature (Nair et al., 2008). Thus, the CVD-grown G in this study was a high-quality SLG. The Raman spectrum of the stacked DLG featured a lower value of I_{2D}/I_G than that of the SLG, with a slight blue-shift of the 2D-band, as revealed in Fig. 1(a), indicative of π–π interactions between the two layers of G (Wang et al., 2008; Hao et al., 2010). In the Raman spectrum of the BiG, the value of I_{2D}/I_G decreased further and the 2D-band shifted further toward higher wavenumber.

Suggesting enhancement of the π–π interaction between the two layers of G after annealing. Furthermore, the transmittance of the BiG at 550 nm of 95.2% was almost consistent with the decrease in transmittance of 2.3% for one layer of G. After treating the BiG through LDPT, the intensity of the D-band increased dramatically, presumably because chemical functionalization through the oxidation process led to shifts in

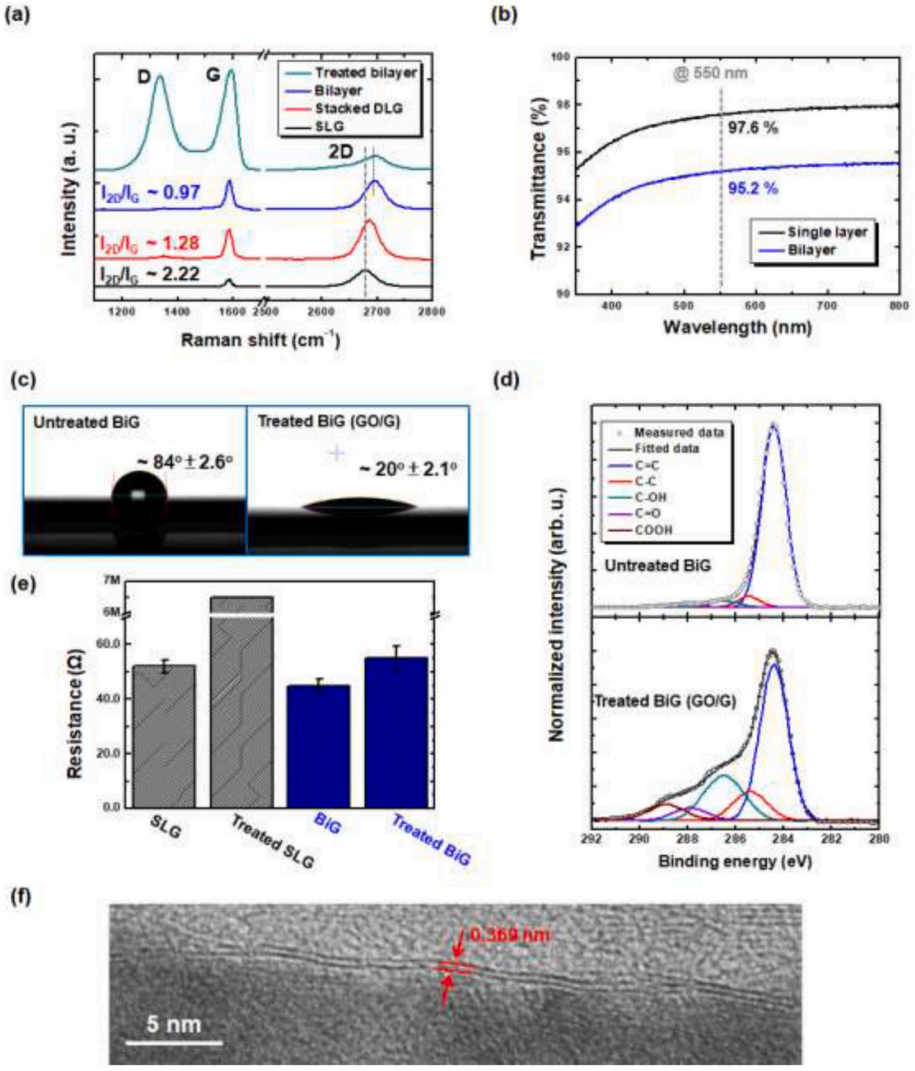

Fig. 1. (a) Raman spectra of the SLG, stacked DLG, BiG, and GO/G structures; (b) transmittance spectra of the SLG and BiG; (c) contact angles of the BiG before and after LDPT; (d) XPS spectra of the BiG before and after LDPT; (e) electrical resistances of the SLG and BiG before and after LDPT; (e) TEM image of the layered structure of GO/G.

the phonon frequency measured by Raman spectroscopy. The I_{2D}/I_G also decreased significantly after LDPT, and a slight upshift was observed indicating p-doping by LDPT, which is consistent with the findings of studies applying oxygen plasma treatment (Childres et al., 2011; Rozada et al., 2014). The CA of the untreated BiG decreased significantly from 84 to 20° after LDPT, as displayed in Fig. 1(c), consistent with hydrophilic properties that may have resulted from the formation of oxidative functional groups on the surface of the BiG. We used XPS to examine the chemical functionalization of the BiG [Fig. 1(d)]. The XPS spectra of the BiG and the treated sample could be deconvoluted to reveal five types of carbon bonding states: sp^2-hybridized C=C bonds at 284.5 eV, sp^3-hybridized C–C bonds at 285.5 eV, C–OH groups at 286.6 eV, C=O groups at 288 eV, and CO_2H groups at 288.9 eV (Krishnamoorthy et al., 2013; Stankovich et al., 2007). Among these bonding states for carbon atoms, the CO_2H groups of the GO sheet were the most important because they could react with amino groups of the probe to form covalent bonds between the GO sheet and the probe units. The content of oxidative functional groups, including C–OH, C=O, and CO_2H groups, increased after LDPT had induced the defect structure, as observed using Raman spectroscopy [Fig. 1(a)]. By comparing the spectra of the BiG and the treated sample, we concluded that the CO_2H groups constituted up to 7.5% of all the functional groups. The percentages of other bonding states were summarized in Table S2. Fig. 1(e) presents plots of the resistance of the devices incorporating the SLG or BiG, before and after applying the LDPT process. The resistances of device with the SLG increased sharply after LDPT. Indeed, the resistance of the treated SLG exceeded several megaohms, indicating that it almost became an electrically insulating material. In contrast, the resistance of the device with the BiG increased only slightly after LDPT. Thus, although the top layer of G had been oxidized to become an insulator, the conductivity of the GO/G sample remained comparable with that of the SLG, suggesting that the bottom layer of G was almost uninfluenced by the LDPT. The morphologies of BiG before and after LDPT were observed by scanning electron microscopy (SEM). The morphology of the BiG layers did not visually change after LDPT (see Fig. S3(a)). The result was consistent with those reported by Felten et al., (2013), who used conventional plasma treatment. The elemental composition of BiG before and after LDPT was also examined by energy-dispersive X-ray spectroscopy (EDS) (see Fig. S3(b)). The BiG samples were prepared on a Cr/Au-deposited Si substrate. The results revealed that the carbon element slightly decreased while the oxygen element increased owing to the oxidation process done by LDPT, which was consistent with the XPS results. Transmission electron microscopy (TEM) measurement was performed to confirm the layered structure of GO/G. As displayed in Fig. 1(f), a two-layer structure was clearly observed, and the spacing between the two layers was approximately 0.369 nm. Given the results in Fig. 1, we concluded that atomic layer oxidation was achieved through LDPT to form a layered structure of GO/G as a transducer. The top layer of GO and the bottom layer of G in the layered structure of GO/G would play roles as biorecognition and electrical response layers, respectively.

3.2. Sensing performance

To examine the immobilization of the probe DNA covalently attached to the GO/G surface, we exposed the GO/G sample to an amino- and FAM (carboxy fluorescein)-modified probe DNA and then investigated its hybridization with the complementary DNA, namely miRNA-21 (Xie et al., 2009; Huang et al., 2012; Felten et al., 2013). In principle, it should have been possible to visualize the attachment of the fluorescent FAM-terminated probe DNA on the GO/G sample after covalent amide bonds had formed between the amino groups of the probe DNA and CO_2H groups on the GO/G surface. In practice, however, due to the quenching effect of G, we could not immediately confirm the immobilization of the probe DNA with GO/G. To restore the fluorescence, we needed to perform hybridization with a complementary DNA to form the duplex, thereby allowing the probe DNA to distance itself from the surface. Fig. 2(a) presents a fluorescence microscopy image of the GO/G/SiO_2 sample after exposure to the amino- and FAM-modified DNA probe and its complementary target; the inset provides an optical image of the sample. The fluorescence observed on the GO/G, highlighted by the dashed lines, confirmed the successful covalent attachment of the probe DNA through the immobilization process. We also evaluated the immobilization process by measuring the variation in resistance when using the probe DNA lacking the FAM unit. The sensor resistance increased after immobilization; its corresponding variation was 9.55%, as displayed in Fig. 2(b), while the resistance of the GO/G sample itself remained almost unchanged in the PBS solution, indicating that the effect of the buffer solution was negligible. We also performed immobilization step as described in section 2.2 onto the SLG, DLG and BiG and measured the resistance variations of them. All the resistance variations of SLG, DLG and BiG after immobilization were much smaller than that of GO/G (see Fig. S4). It is considered that there is no strong chemically covalent bond between G and probe leading to an easy loss of probe during the washing steps after immobilization. Therefore, there was only a few probes on the surface of G resulting in a tiny effect on its conductivity. It may be also noted that the resistances decreased in the cases of SLG, DLG and BiG, which are not the main topic in this study, and we will not discuss it. The results suggest that the attachment of the probe DNA onto the GO surface (top layer) led to a variation in the resistance of the G layer (bottom layer) as a result of π–π interactions. Therefore, we expected that the resistance of the GO/G sample would further change after performing the subsequent target hybridization. In addition, the stability of the GO/G-based chemiresistive sensors, which were ready for miRNA-21 detection, were evaluated by measuring the resistance variation after immobilization. Before each measurement, the sensors were stored in a PBS solution. The resistances remained the same even after seven-day storage, revealing the good stability of the sensor fabricated in this work (see Fig. S5).

Fig. 3(a) presents the response of the sensor after hybridization with its complementary miRNA-21 at various concentrations. The sensor's response increased linearly upon increasing the concentration of miRNA-21 from 10 pM to 100 nM. A linear fit yielded the equation

$$Y = 2.001 \log X + 22.297 \quad (2)$$

Where X and Y are the concentration of the target and the response of the sensor, respectively, with a linearity (R^2) of 0.986. The LOD of the complementary miRNA-21 for the GO/G-based chemiresistive biosensor was 14.6 pM, estimated as three times the standard deviation from the mean of the blank (Jou et al., 2017). Table 1 shows a comparison of the target detection methods. Although some methods show very low LODs, the LOD in this study is comparable with or even better than those of most of the other methods. The LOD in this study can be further improved by optimizing the interdigitated electrode and enhancing the π-π interaction between the graphene layers, which are the focuses of our next study. We measured the Hall effect to explore the reason behind the linear increase in resistance with respect to the target concentration. As revealed in Fig. 4, both the mobility and the carrier concentration decreased upon increasing the target concentration. The presence of electron-rich molecules (i.e., those possessing net negative charge) can induce n-doping effects in G (Andronescu et al., 2017; Brndiarova et al., 2019). In our present system, the miRNA-21 attached to the surface of the top GO layer had net negative charge, leading to interfacial charge transfer to neutralize the hole carrier concentration of the p-type bottom G layer through π–π interactions (Zhang et al., 2012). As a result, the carrier concentration decreased upon increasing the target concentration.

of miRNA-21. The mobility also decreased upon increasing the concentration of the target. Because G is a typical 2D material and only one atom thick, it is very sensitive to nearby foreign atoms or molecules, leading to carrier scattering within it. Therefore, the mobility of the GO/G decreased after attachment of the target miRNA-21, resulting in

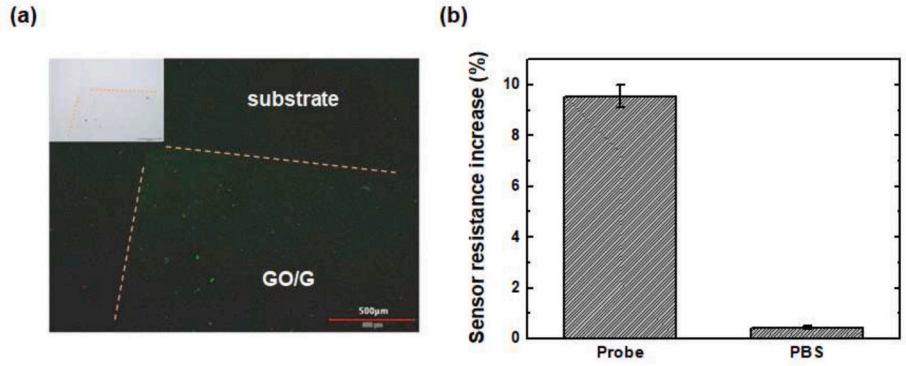

Fig. 2. (a) Fluorescence microscopy image of the GO/G sample after exposure to the amino- and FAM-modified DNA probe; inset: optical image of the sample. (b) Increases in the sensor resistance after immobilization of the probe and in PBS.

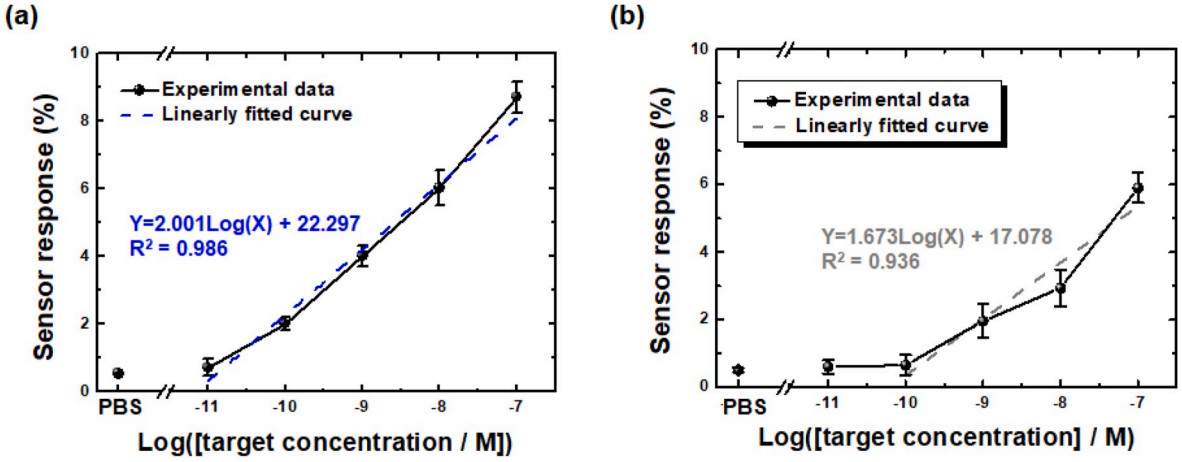

Fig. 3. Responses of the (a) BiG and (b) stacked DLG subjected to LDPT, plotted with respect to the concentration of the target miRNA-21.

Table 1
The comparison of the target detection methods.

Method	Materials	Target	LOD	Linear range	Linearity (R^2)	Ref.
Fluorescent resonance energy transfer	DNA-AgNCs and Cy5.5	miRNA-21	4 pM	0.02-100 nM	0.9945	Nasirian et al. (2020)
Fluorescent resonance energy transfer	QDs/GO	miRNA-21	1 pM	1 pM-1 nM	0.9972	Huang et al. (2017)
		miRNA-155			0.9957	
Fluorescent resonance energy transfer	CdTe@CdS core-shell QDs	miRNA-122	0.2 nM	5-270 nM	0.9979	Xiang et al. (2020)
		miRNA-199a/b-3p	0.5 nM	10-350 nM	0.9933	
Resonance light scattering	AuNPs	miRNA-21	2.2 pM	10-200 nM	0.9981	Ren et al. (2016)
cyclic enzymatic amplification	Polydopamine nanosphere	miRNA-21	55 fM	2.5-100 nM	0.992	Li et al. (2020)
Colorimetric	Graphene/AuNPs	miRNA-21	3.2 nM	10 nM-0.98 μM	0.9984	Zhao et al. (2016)
Colorimetric	AuNPs/PolyA	miRNA-155	10 pM	0.01-200 nM	N/A	Wang et al. (2015)
		miRNA-196a				
Electrochemical differential pulse voltammetry	AuNPs/GO	miRNA-155	0.6 fM	2 fM-8 pM	0.9945	Azimzadeh et al. (2016)
Electrochemical amperometry	SWCNTs	DNA	71 pM	0.25-1.75 nM	0.9907	Fottunati et al. (2019)
Electrochemical impedance spectroscopy	GO	miRNA-34a	28.1 pM	~40-150 pM	0.9756	Congur et al. (2015)
Chemiresistive	N-MWCNTs	DNA of AIV H5N1	~20 pM	20-2000 pM	N/A	Fu et al. (2017)
	Sc-SWCNTs		~2 pM	2-200 pM		
Chemiresistive	GO/G	miRNA-21	14.6 pM	10 pM-100 nM	0.986	This work

carrier scattering in the bottom layer of G through π–π interactions. According to the van der Pauw equation

$$R \propto 1/\mu n \quad (3)$$

The resistivity (R) is proportional to the inverse of the product of the carrier mobility (μ) and the carrier concentration (n). Both factors contributed to the increase in the resistivity of the GO/G sample (see Fig. S6); therefore, measurement of the variation in resistance of GO/G in a simple chemiresistive device would appear to be a very promising means of detecting miRNA-21. Both the mobility and the carrier concentration of the bottom G layer changed significantly after attachment of the biomolecule, the result of π–π interactions. To confirm this effect, the stacked DLG (without annealing) was subjected to LDPT (under the same conditions as the BiG) and used as the active layer for detecting miRNA-21. Hereafter, we call this structure the "stacked GO/G." Fig. 3 (b) presents the response of the stacked GO/G sensor with respect to the concentration of the target. Although the response of the stacked GO/G sensor did also increase upon increasing the concentration of the target, its linear range had shrunk (i.e., from 100 pM to 100 nM). In addition,

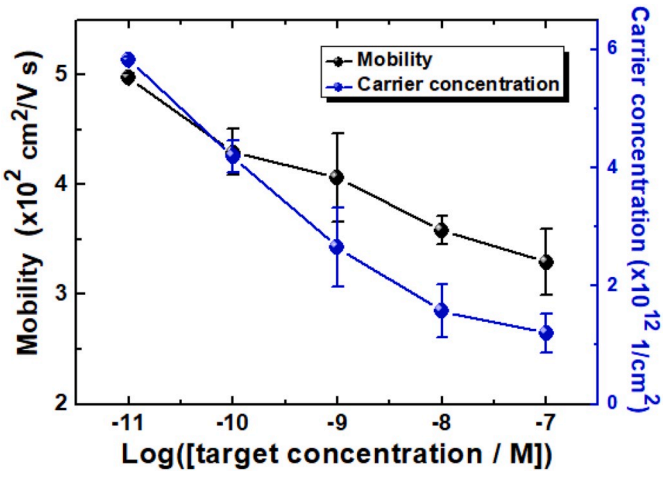

Fig. 4. Carrier mobility and concentration plotted with respect to the concentration of the target miRNA-21, as obtained through Hall measurements.

linear fitting indicated that the sensitivity (i.e., the slope) and linearity (R^2) were worse than those of the GO/G sensor. These findings suggest that the response of the bottom G layer became less sensitive when the π–π interactions between the two layers became weaker, as displayed in Fig. 1(a). Moreover, we also prepared trilayer G (i.e., G/G/G) and subjected it to LDPT under the same conditions as those for the BiG to become GO/G/G, then investigated its sensing performance. The sensor response of GO/G/G toward miRNA-21 at 100 nM was significantly weaker than that of GO/G (see Fig. S7). Thus, by adding an additional layer of G under the GO sheet, the sensor became less sensitive. We suspect that the influence of the attachment of miRNA-21 on the doping effect and carrier mobility became less significant when using the GO/G/G structure because there were more hole carriers and more possible paths for the carriers to be transported in the bottom two layers of G.

3.3. Sensor selectivity

Selective sensing is required for the practical applications of any biosensor. We evaluated the discrimination ability of our GO/G-based chemiresistive biosensor through its responses to various oligonucleotides, including single- and four-base-mismatched and other non-complementary miRNAs, all at the same concentration of 100 nM in PBS. As presented in Fig. 5, the response of the sensor toward its complementary miRNA was much higher than those toward the other mismatched sequences; in other words, our biosensor could discriminate complementary miRNA-21 as its target with high selectivity. In addition, we investigated the detection of miRNA-21 at a concentration of 100 nM in both HSA and BSA (undiluted) to evaluate the effects of a complex matrix. As displayed in Fig. 6, the responses of the sensor toward miRNA-21 in solutions of both HSA and BSA were almost identical to that in PBS. Thus, our sensor exhibited high selectivity and could ignore interference, suggesting that it might be applicable for analysis of real specimens.

4. Conclusions

We have prepared a layered GO/G structure, through an atomic layer oxidation process (LDPT) on BiG, as a simple chemiresitive biosensor for the detection of circulating miRNA-21 and early cancer diagnosis. The oxidized surface of the top layer of GO enabled covalent attachment of the probe DNA and subsequent hybridization with its target miRNA-21. The response of the biosensor increased linearly upon increasing the concentration of target miRNA-21, with a linearity (R^2) of 0.986 and an LOD of 14.6 pM. Hall measurements revealed that hybridization of the target decreased both the carrier mobility and the carrier concentration

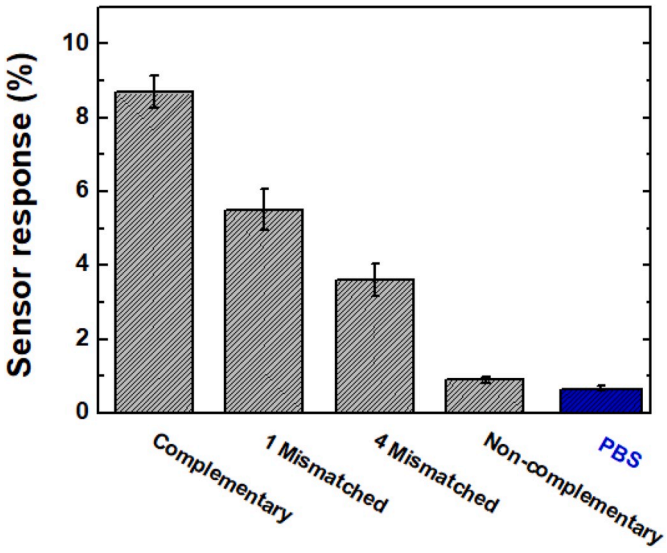

Fig. 5. Responses of the GO/G-based chemiresistive biosensor toward the complementary target miRNA-21 and single- and four-base-mismatched and non-complementary miRNAs (each at a concentration of 100 nM in PBS), as well as that toward PBS itself.

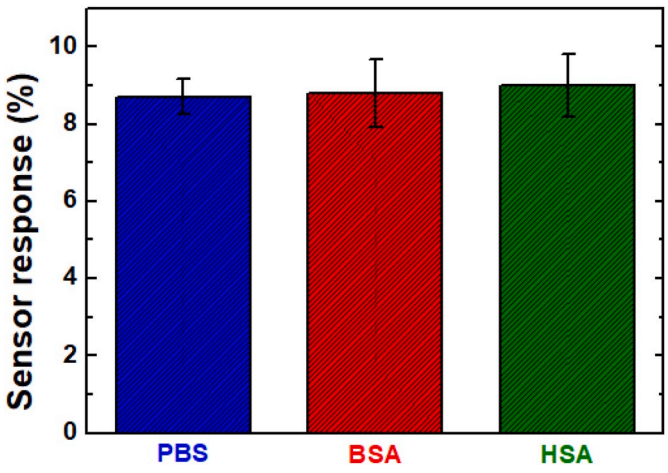

Fig. 6. Responses of the GO/G-based chemiresistive biosensor toward its complementary target miRNA-21 (100 nM) in PBS, HSA, and BSA.

of the bottom layer of G, the result of π–π interactions. Both of these decreases contributed to the increase in resistivity, which we could measure simply, of the GO/G-based chemiresistive biosensor. Our biosensor displayed high selectivity for its target against several other miRNA sequences, and ignored any potential interference from the components of HSA and BSA solutions. The high sensitivity, selectivity, repeatability, and simplicity of our GO/G-based chemiresistive biosensor all suggest that it has great potential for use as a platform for the detection of miRNA-21. Nevertheless, this biosensor requires further clinical validation and miniaturization if it is to be exploited in autonomous point-of-care testing devices. Moreover, we suggest that the geometric size of the interdigitated electrode could be further optimized to enhance the sensing performance.

Declaration of competing interest

The authors declare no competing financial interest.

CRediT authorship contribution statement

Chi-Hsien Huang: Conceptualization, Methodology, Writing - original draft, Writing - review & editing. **Tzu-Ting Huang:** Methodology, Validation, Writing - original draft. **Chia-Heng Chiang:** Methodology, Validation, Formal analysis. **Wei-Ting Huang:** Investigation, Visualization. **Yi-Ting Lin:** Investigation.

Acknowledgment

This study was funded by the Ministry of Science and Technology of Taiwan under grant number 107-2221-E-131-006-MY3.

Appendix A. Supplementary data

Supplementary data to this article can be found online at https://doi.org/10.1016/j.bios.2020.112320.

References

Andronescu, C., Schuhmann, W., 2017. Curr. Opin. Electrochem. 3 (1), 11–17.
Azimzadeh, M., Rahaie, M., Nasirizadeh, N., Ashtari, K., Naderi-Manesh, H., 2016. Biosens. Bioelectron. 77, 99–106.
Brndiarova, J., Siffalovic, P., Hulman, M., Kalosi, A., Bodik, M., Skakalova, V., Micusik, M., Markovic, Z., Majkova, E., Frohlich, K., 2019. J. Appl. Phys. 126 (21), 214303.
Casiraghi, C., Pisana, S., 2007. Appl. Phys. Lett. 91 (23), 233108.
Cheng, H.E., Wang, Y.Y., Wu, P.C., Huang, C.H., 2016. Surf. Coating. Technol. 303, 170–175.
Cheng, D., Yang, L., Li, X., Zhou, J., Chen, Q., Yan, S., Li, N., Chu, M., Dong, Y., Xie, Z., Zhang, C., 2017. J. Electrochem. Soc. 164 (6), H345–H351.
Childres, I., Jauregui, L.A., Tian, J., Chen, Y.P., 2011. New J. Phys. 13, 025008.
Congur, G., Eksin, E., Erdem, A., 2015. Electrochim. Acta 172, 20–27.
Dong, X., Shi, Y., Huang, W., Chen, P., Li, L.J., 2010. Adv. Mater. 22 (14), 1649–1653.
Felten, A., Flavel, B.S., Britnell, L., Eckmann, A., Louette, P., Pireaux, J.J., Hirtz, M., Krupke, R., Casiraghi, C., 2013. Small 9 (4), 631–639.
Fottunati, S., Rozzi, A., Curti, F., Giannetto, M., Corradini, R., Careri, M., 2019. Sensors 19 (3), 588.
Fu, Y., Romay, V., Liu, Y., Ibarlucea, B., Baraban, L., Khavrus, V., Oswald, S., Bachmatiuk, A., Ibrahim, I., Rümmei, M., Gemming, T., Bezugly, V., Cuniberti, G., 2017. Sensor. Actuator. B Chem. 249, 691–699.
Hao, Y., Wang, Y., Wang, L., Ni, Z., Wang, R., Koo, C.K., Shen, Z., Thong, J.T.L., 2010. Small 6 (2), 195–200.
Hong, C.Y., Chen, X., Liu, T., Li, J., Yang, H.H., Chen, J.H., Chen, G.N., 2013. Biosens. Bioelectron. 50, 132–136.
Huang, P.J.J., Liu, J., 2012. Small 8, 977–983.
Huang, C.H., Lu, T.H., 2018. Surf. Coating. Technol. 350, 1085–1090.
Huang, Y., Dong, X., Liu, Y., Li, L.J., Chen, P., 2011. J. Mater. Chem. 21 (33), 12358–12362.
Huang, C.H., Su, C.Y., Lai, C.S., Li, Y.C., Samuakwa, S., 2014. Carbon 73, 244–251.
Huang, R., Liao, Y., Zhou, X., Fu, Y., Xing, D., 2017. Sensor. Actuator. B Chem. 247, 505–513.
Jansson, M.D., Lund, A.H., 2012. Mol. Oncol. 6 (5), 590–610.
Jou, A.F.J., Chen, Y.J., Li, Y., Chang, Y.F., Lee, J.J., Liao, A.T., Ho, J.A.A., 2017. Electrochim. Acta 236, 190–197.
Justino, C.I.L., Gomes, A.R., Freitas, A.C., Duarte, A.C., Rocha-Santos, T.A.P., 2017. Trends Anal. Chem. 91, 53–66.
Kim, S.W., Li, Z., Moore, P.S., Monaghan, A.P., Chang, Y., Nichols, M., John, B., 2010. Nucleic Acids Res. 38 (7), e98.
Krishnamoorthy, K., Veerapandian, M., Yun, K., Kim, S.J., 2013. Carbon 53, 38–49.
Li, Q., Zhou, S., Zhang, T., Zheng, B., Tang, H., 2020. Biosens. Bioelectron. 150, 111866.
Liang, B., Fang, L., Yang, G., Hu, Y., Guo, X., Ye, X., 2013. Biosens. Bioelectron. 43, 131–136.
Nair, R.R., Grigorenko, A.N., Novoselov, K.S., Booth, T.J., Stauber, T., Peres, N.M.R., Geim, A.K., 2008. Science 320 (5881), 1308.
Nasirian, V., Shamsipur, M., Molaabasi, F., Mansouri, K., Sarparast, M., Salim, V., Kashanian, S., 2020. Sensor. Actuator. B Chem. 308, 127673.
Ni, Z., Wang, Y., Yu, Ting, Shen, Z., 2008. Nano Res 1 (4), 273–291.
Novoselov, K.S., Geim, A.K., Morozov, S.V., Jiang, D., Zhang, Y., Dubonos, S.V., Grigorieva, I.V., Firsov, A.A., 2004. Science 306 (5696), 666–669.
Ouyang, T., Liu, Z., Hang, Z., Ge, Q., 2019. Anal. Chem. 91 (5), 3179–3186.
Park, C.S., Yoon, H., Kwon, O.S., 2016. J. Ind. Eng. Chem. 38, 13–22.
Qian, L., Li, Q., Baryeh, K., Qiu, W., Li, K., Zhang, L., Xu, D., Liu, W., Brand, R.E., Zhang, X., 2019. Transl. Res. 213, 67–89.
Ren, M., Wang, S., Cai, C., Chen, C., Chen, X., 2016. RSC Adv. 6, 83078–83083.
Rozada, R., Solís-Fernández, P., Paredes, J.I., Martínez-Alonso, A., Ago, H., Tascón, J.M. D., 2014. Carbon 79, 664–669.
Salahandish, R., Ghaffarinejad, A., Omidinia, E., Zargartalebi, H., Majidzadeh-A, K., Naghib, S.M., Sanati-Nezhad, A., 2018. Biosens. Bioelectron. 120, 129–136.
Stankovich, S., Dikin, D.A., Piner, R.D., Kohlhaas, K.A., Kleinhammes, A., Jia, Y., Wu, Y., Nguyen, S.T., Ruoff, R.S., 2007. Carbon 45 (7), 1558–1565.
Wang, Y., Ni, Z., Yu, T., Shen, Z., Wang, H., Wu, Y., Chen, W., Wee, A.T.S., 2008. J. Phys. Chem. 112 (29), 10637–10640.
Wang, C., Zhang, H., Zeng, D., Sun, W., Zhang, H., Aldalbahi, A., Mi, X., 2015. Nanoscale 7 (38), 15822–15829.
Wang, J., Lu, J., Dong, S., Zhu, N., Gyimah, E., Wang, K., Li, Yong, Zhang, Z., 2019a. Biosens. Bioelectron. 130, 81–87.
Wang, W., Su, H., Wu, Y., Zhou, T., Li, T., 2019b. J. Electrochem. Soc. 166 (6), B505.
Xia, N., Zhang, Y.J., Wei, X., Huang, Y.P., Liu, L., 2015. Anal. Chim. Acta 878, 95–101.
Xiang, L., Zhang, F., Feng, J., Chen, C., Cai, C., 2020. Microchim. Acta 187, 134.
Xie, L., Ling, X., Fang, Y., Zhang, J., Liu, Z., 2009. J. Am. Chem. Soc. 131, 9890–9891.
Zhang, Z., Huang, H., Yang, X., Zang, L., 2012. J. Phys. Chem. Lett. 2, 2897–2905.
Zhang, C., Miao, P., Sun, M., Yan, M., Liu, H., 2019. Small 15 (38), 1901867.
Zhao, H., Qu, Y., Yuan, F., Quan, X., 2016. Anal. Methods 8 (9), 2005–2012.